ISSN 1349-1113
JAXA-RR-07-030E

JAXA Research and Development Report

Application of the Wake Integral Method to CFD Data

Makoto UENO and Junichi AKATSUKA

February 2008

Japan Aerospace Exploration Agency

Application of the Wake Integral Method to CFD Data

Makoto Ueno* and Junichi Akatsuka*

Abstract

The wake integral method, a method that analyzes aerodynamic forces by integral in the wake of a model, was applied to three-dimensional CFD data and a quantitative assessment of aerodynamic forces produced by airplane elements was performed. The method allows the drag force exerted on a body to be decomposed into profile and induced drag components, and provides their distributions. By using this method, a designer can expect to obtain insight into aerodynamic drag production factors from CFD data and wind tunnel wake traverse data. In this study, CFD spatial data of a rectangular NACA0012 section wing and the DLR F6 wing-body model were analyzed and the insights gained into the aerodynamic force distributions and drag were examined.

Keywords : *Wake Integral Method, Computational Fluid Dynamics*

概要

物体後流内部の物理量を積分して抵抗と揚力を算出する手法（Wake Integral Method）を三次元ＣＦＤデータに適用し、飛行機の各要素が抵抗全体に及ぼす影響の度合いの定量的な評価を行った。この手法では抵抗を発生要因によって Profile Drag と Induced Drag に分解し、さらに空気力の定量的な分布を得ることができる。従って、ＣＦＤにおいても風洞試験データにおいても同様に抵抗発生要因を特定し、設計にフィードバックすることが期待できる。本研究では NACA0012 断面を有する矩形翼と翼胴形態である DLR F6 模型に対する解析を行い、解析結果から得られる知見について考察を行った。

Nomenclature

CD	drag coefficient
CDi	induced drag coefficient
CDp	profile drag coefficient
CL	lift coefficient
Cdi	sectional induced drag coefficient
Cdp	sectional profile drag coefficient
Cl	sectional lift coefficient
D	drag force
L	lift force
M_∞	freestream Mach number
P , P_∞	local and freestream pressures
P_t , $P_{t\infty}$	local and freestream total pressures
R	gas constant
S	control volume surface area
U_∞	freestream velocity
W_A	integral area over the model wake region
l	sectional lift force
$\vec{n}$	surface outward unit normal vector, (n_x, n_y, n_z)
s , Δs	local and purturbation entropy
$\vec{u}$	velocity vector, (u, v, w)
x , y , z	coordinate in freestream, sidewise, and transverse directions
x_c	coordinate-x based on chord length
$\Gamma(y)$	circulation distribution
γ	ratio of specific heats
μ_l , μ_t	dynamic and eddy viscosity
ρ , ρ_∞	local and freestream density
ξ	x-component of vorticity vector
ψ	two-dimensional stream function in Trefftz plane

1 Introduction

In general, the aerodynamic forces exerted on a wind tunnel test model are obtained using an aerodynamic force balance, which measures the integrals of pressure and friction on the model's surface and gives a near-field representation of the aerodynamic forces. Conventional methods of extracting aerodynamic force coefficients from CFD results are also based on this near-field representation.

---

* Researcher, Wind Tunnel Technology Center, Institute of Aerospace Technology.

There is also an alternative representation called the far-field representation, in which the aerodynamic forces are expressed as the balance of momentum over a control volume around the model. Although the classical far-field method requires the integral of physical properties over the entire surface of the control volume, Betz[2)] succeeded in confining the integral to the inside the model's wake for two-dimensional wind tunnel drag measurement, and the theory was extended to three-dimensional wind tunnel testing by Maskell[3)]. Maskell's method was epoch-making as it required planar traversing measurement only within the wake of a wind tunnel model to acquire aerodynamic drag and lift forces (Fig. 1). Maskell's method was subsequently improved by Cummings[4)]. On the other hand, the classical far-field method was extended to compressible flow[5)] and used to avoid CFD drag error due to conventional surface integral.

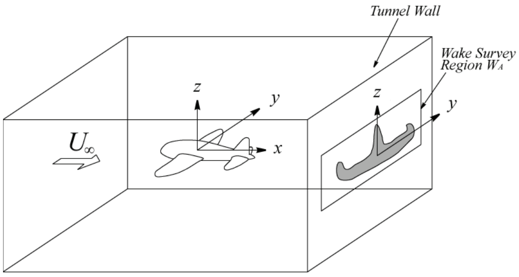

Fig. 1 Image of wake integral control volume.

Recently, Kusunose[6)] and Méheut and Bailly[7)] have independently integrated these methods. Although wake integral had not previously been popular in wind tunnel testing except for two-dimensional wing section drag measurement, it became practical after their studies because their methods cover a wide enough range of wind tunnel conditions to be applicable to conventional transport airplanes, and laborious quantitative flow surveys are confined only to inside the wake.

This method, which is called the wake integral method (WIM), is an attractive tool both for wind tunnel testing and CFD analysis, mainly because it can render the spanwise distribution of drag and lift visible quantitatively, and this knowledge of the aerodynamic force distribution is useful for drag source identification. Additionally, it can decompose drag into induced drag and profile drag components. Drag decomposition gives insight into the flow physics necessary for design improvement.

Although commercial and cost pressures have been driving a reduction in airplane development time, wind tunnel test time has been growing due to the increasing complexity and expanding performance envelopes of aircraft (Fig. 2). Although the conventional wind tunnel force balance is a vital tool for measuring aerodynamic force, the balance outputs are only the integrals of the aerodynamic forces exerted on the model's surface and additional flow visualization studies are required to explore the physical phenomena around the model. Moreover, these visualization methods generally provide only qualitative information, and nothing provides information about the impact of the phenomena on aerodynamic drag. On the other hand, while CFD can provide quantitative surface force distributions, the results still need to be validated by wind tunnel data, and it is difficult for wind tunnel tests to provide completely correspondent information to the CFD data on the model's surface.

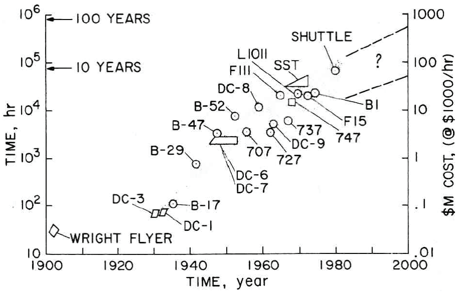

Fig. 2 Total wind tunnel test hours for development of various aircraft[1)].

The WIM can be applied equivalently to both wind tunnel and CFD data, and its output directly expresses the aerodynamic forces shed from each component of the aircraft. One of the authors made an effort to apply the method to low speed wind tunnel tests[8)9)]. Then, corresponding to recent airplane development activities in Japan, the authors are now developing a sophisticated wake integral system involving wind tunnel testing and CFD. In this study, wake integral computer software was developed based on Kusunose's method[6)] and verified by application to CFD data. Analyses were performed of the spatial data of a simple rectangular NACA0012 section wing and the transonic DLR-F6. Insight into aerodynamic forces directly related to aerodynamic phenomena was thereby acquired, and it was demonstrated that the WIM representation is an effective interpretation of CFD data.

2 Wake Integral Method

2.1 Momentum Balance

The WIM method is described by Kusunose6) in detail and it is introduced briefly in this section. The aerodynamic forces exerted on the body of a model are interpreted as momentum balance over a control volume that includes the aerodynamic body immersed in the fluid. The drag and lift forces acting on the body are written as

$$D = -\iint_S \rho u(\vec{u} \cdot \vec{n})dydz \\ -\iint_S (P - P_\infty)n_x dydz$$

and

$$L = -\iint_S \rho w(\vec{u} \cdot \vec{n})dydz \\ -\iint_S (P - P_\infty)n_z dydz ,$$

respectively. The integral area S is the surface of a control volume which contains the body.

When the small perturbation assumption is applied to the velocity, pressure, and density of the fluid, the aerodynamic drag and lift exerted on the body can be expressed in integral forms only in the wake area, W_A, as the following equations6). In these equations, the installed power effect (thrust) is omitted.

$$D = \iint_{W_A} P_\infty \frac{\Delta s}{R} dydz \\ + \frac{\rho_\infty}{2} \iint_{W_A} \psi \xi dydz \\ - \iint_{W_A} \frac{P_\infty}{2} \left(\frac{\Delta s}{R} \right)^2 dydz + O(\Delta^3)$$

$$L = \rho_\infty U_\infty \iint_{W_A} y \xi ds \\ - \rho_\infty U_\infty{}^2 (1 - M_\infty{}^2) \iint_{W_A} \frac{w}{U_\infty} \frac{\Delta u}{U_\infty} ds \\ + M_\infty{}^2 \frac{\gamma P_\infty}{R} \iint_{W_A} \frac{w}{U_\infty} \Delta s ds + O(\Delta^3)$$

In the drag expression, the first term corresponds to the profile drag and the second term is the induced drag. The third term is a second-order correction term of the profile drag.

2.2 Force Distribution

The drag and lift distributions can be acquired as the integrands of the wake integral representation of drag and lift forces. When the integrands are plotted, the distribution of aerodynamic force "fragments" can be shown as in an example of Fig. 3. When they are integrated toward the vertical direction, span-wise distributions are acquired6).

However, the integrand of the first term of the lift equation is an exception and it does not correspond to lift distribution, but just the total of it. Even if it is integrated to the vertical direction, span-wise distribution of the lift can not be plotted because the lift at a wing section have to be computed based on the planar wake approximation (Fig. 4), and it requires integral of the vorticity over the entire area of one side of the wake plane cut by the plane crossing the wing section.

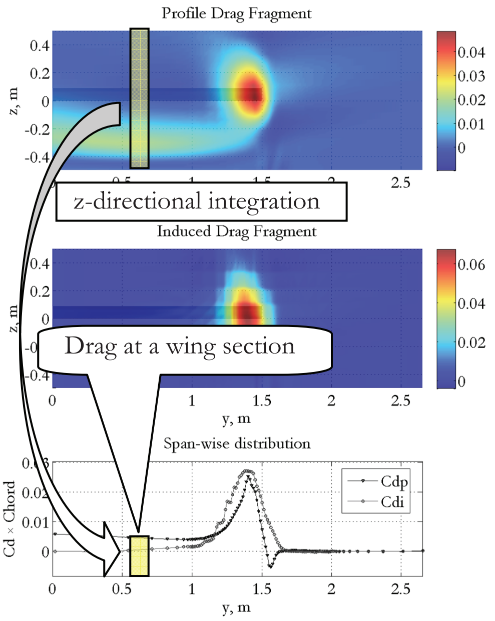

Fig. 3 Z-directional integration of force fragment and acquired span-wise distribution.

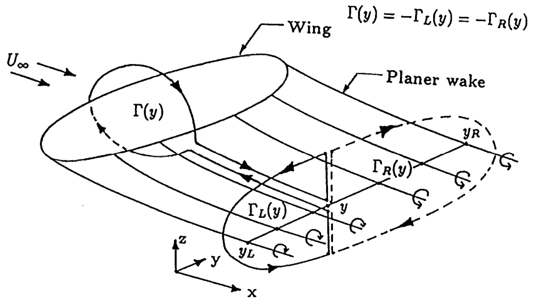

Fig. 4 **Planar wake and circulation around a wing⁶⁾.**

To acquire an integrand which can be integrated with the same manner as the other aerodynamic force components, lift equation should be transformed. Then, the first term of the lift equation was transformed as follows by using integration by parts. This representation of lift realizes lift fragment, *l*, which can be integrated simply as same as the rest of force components.

$$
\begin{aligned}
L &= \iint_{W_A} \rho_\infty U_\infty y\xi dydz \\
&= \int_{y_{\min}}^{y_{\max}} \int_{z_{\min}}^{z_{\max}} \rho_\infty U_\infty y\xi dzdy \\
&= \int_{y_{\min}}^{y_{\max}} y\left(\int_{z_{\min}}^{z_{\max}} \rho_\infty U_\infty \xi dz\right)dy \\
&= -\int_{y_{\min}}^{y_{\max}} \rho_\infty U_\infty y\frac{d\Gamma(y)}{dy}dy, \left(\Gamma(y) = -\int_{y}^{y_{\max}}\left(\int_{z_{\min}}^{z_{\max}} \xi dz\right)dy_1\right) \\
&= \left\{-\left[\rho_\infty U_\infty y\Gamma(y)\right]_{y_{\min}}^{y_{\max}} + \int_{y_{\min}}^{y_{\max}} \rho_\infty U_\infty \Gamma(y)dy\right\} \\
&= \int_{y_{\min}}^{y_{\max}} \rho_\infty U_\infty \Gamma(y)dy \\
&\quad , \begin{pmatrix} \because \Gamma(y_{\min}) = \Gamma(y_{\max}) = 0 \text{ for full-span,} \\ y_{\min} = 0 \text{ for half-span} \end{pmatrix} \\
&= \int_{y_{\min}}^{y_{\max}} \int_{y}^{y_{\max}} \left(\int_{z_{\min}}^{z_{\max}} \rho_\infty U_\infty \xi dz\right)dy_1 dy \\
&= \int_{y_{\min}}^{y_{\max}} \int_{z_{\min}}^{z_{\max}} \left(\int_{y}^{y_{\max}} \rho_\infty U_\infty \xi dy_1\right)dzdy \\
&= \int_{y_{\min}}^{y_{\max}} \int_{z_{\min}}^{z_{\max}} (l)dzdy
\end{aligned}
$$

3 NACA0012 Rectangular Wing at Low-Speed

3.1 Model Description

As a first attempt to validate our WIM software, a semi-span wing with a NACA0012 section and a semi-span aspect ratio of 2.5 was selected as a simple rectangular wing model. The chord length was 600 mm, and the wing tip was cut straight. The data were reflected against the symmetric plane to form a symmetric data set because the software cannot handle the wall boundary condition at present.

3.2 CFD Conditions

CFD analysis[10)] was performed using a structured multi-block mesh as the computational mesh, with a free-stream velocity of 60 m/s and a Reynolds number based on chord length of 1.8×10^6. The flow field was computed at angles of attack of 6, 10, and 12 deg.

3.3 Wake Integral Conditions

Wake survey planes were set perpendicular to the free-stream direction at distances x_c = 0.0, 0.1, 0.2, 0.5, 1.0, 2.0, 3.0, 4.0, 5.0, 6.0, 8.0, 10.0 downstream of the wing trailing edge. The distance x_c is based on chord length.

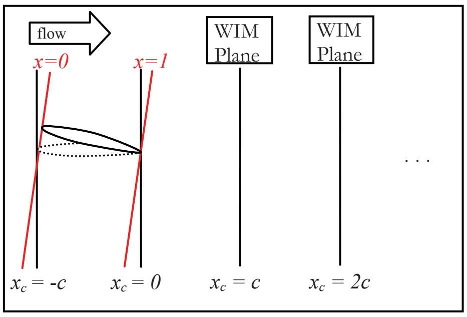

Fig. 5 **WIM analysis planes.**

The WIM is based on the assumption that the total pressure of the flow upstream of the model is uniform. It is natural that a total pressure loss is observed at planes downstream and this should be integrated to compute the drag force. However, in actual CFD spatial data, the total pressure is sometimes not uniform due to numerical errors. In this CFD analysis, the boundary conditions were determined by the velocity of the freestream and small total pressure error was brought into. Total pressure distributions at specific stations along the free-stream flow are plotted in Fig. 6. In the figure, normalized total pressure distributions in z-direction at some transverse planes perpendicular to the freestream are aligned at each section. Scale of the pressure in the plane at x_c = 1.0 is written on the top of the graph. Total pressure variations in the normal direction are observed. Although those errors are very small values, integrated values cannot be ignored. Therefore, the larger the wake integral area, the greater the drag error will be.

To avoid this error, data from 1.5 chords upstream of the trailing edge were subtracted from the wake integral data in advance of the wake integration.

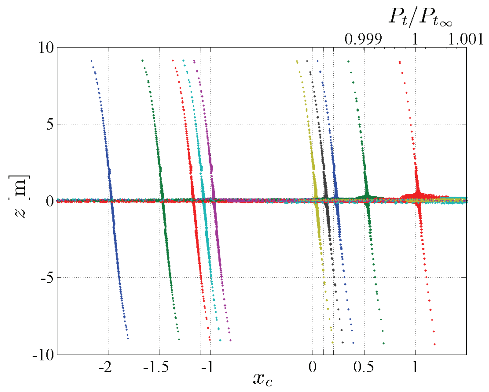

Fig. 6 Total pressure distribution around the model.

3.4 Analysis Results

3.4.1 Total Value

The results of the analysis at each angle of attack are tabulated in Table 1 to Table 3, and are presented graphically in Fig. 7 to Fig. 9. In these tables and the figures, "near-field" refers to the conventional surface integral values. Additionally, the profile drag CDp in the tables is the sum of the first-order approximation CDp1 and the second-order correction term CDp2.

It is seen that the lift and drag predicted by the WIM are very close to the surface integral values. Additionally, except for an area within one chord length downstream of the trailing edge, the computed lift and total drag show hardly any dependency on the location of the integral surface.

Regarding drag component decomposition, it is interesting that induced drag CDi is gradually replaced by profile drag CDp while the total drag remains constant. This phenomenon, namely that induced drag is eventually replaced with profile drag at an infinite distance downstream, is predicted by Yates and Donaldson[11]. However, they also noted that "both theoretical estimates and observations indicate that several miles are required for wake decay" for conventional take off and land (CTOL) aircraft. Therefore, the rate of the replacement in this analysis might be too large in comparison with the prediction, and it is caused by the numerical viscosity peculiar to CFD analysis as indicated by Destarac[12].

Table 1 Variations of drag and lift coefficients of a NACA0012 wing model due to the wake integral stations.

AoA = 6 deg	Wake Integral Station (x chords departed from the end of the wing section)										
	0	0.1	0.2	0.5	1	2	3	4	5	6	8	10
CL	-	4.44E-01	4.44E-01	4.44E-01	4.44E-01	4.41E-01	4.42E-01	4.43E-01	4.46E-01	4.49E-01	4.53E-01	4.58E-01
CDp1	-	1.37E-02	1.15E-02	1.12E-02	1.07E-02	1.02E-02	1.02E-02	1.04E-02	1.06E-02	1.07E-02	1.09E-02	1.14E-02
CDp2	-	-4.98E-05	-3.91E-05	-2.54E-05	-1.75E-05	-9.80E-06	-6.54E-06	-4.80E-06	-3.80E-06	-3.16E-06	-2.59E-06	-2.39E-06
CDp	-	1.36E-02	1.15E-02	1.12E-02	1.07E-02	1.02E-02	1.02E-02	1.04E-02	1.06E-02	1.07E-02	1.09E-02	1.14E-02
CDi	-	1.21E-02	1.22E-02	1.21E-02	1.20E-02	1.15E-02	1.12E-02	1.09E-02	1.06E-02	1.04E-02	1.01E-02	9.66E-03
CD	-	2.58E-02	2.37E-02	2.33E-02	2.26E-02	2.18E-02	2.14E-02	2.12E-02	2.12E-02	2.11E-02	2.10E-02	2.11E-02
CL(near-field)	4.47E-01	4.47E-01	4.47E-01	4.47E-01	4.47E-01	4.47E-01	4.47E-01	4.47E-01	4.47E-01	4.47E-01	4.47E-01	4.47E-01
CD(near-field)	2.31E-02	2.31E-02	2.31E-02	2.31E-02	2.31E-02	2.31E-02	2.31E-02	2.31E-02	2.31E-02	2.31E-02	2.31E-02	2.31E-02
CL(%)		99.47	99.47	99.30	99.34	98.79	98.89	99.10	99.86	100.44	101.48	102.40
CDp(%)		59.00	49.84	48.36	46.16	44.29	44.28	44.99	45.75	46.38	47.41	49.43
CDi(%)		52.55	52.69	52.53	51.80	49.97	48.42	47.01	46.06	44.97	43.57	41.87
CD(%)		111.56	102.53	100.88	97.96	94.26	92.69	92.00	91.81	91.35	90.98	91.30

Table 2 Variations of drag and lift coefficients of a NACA0012 wing model due to the wake integral stations.

AoA = 10 deg	Wake Integral Station (x chords departed from the end of the wing section)										
	0	0.1	0.2	0.5	1	2	3	4	5	6	8	10
CL	7.43E-01	7.41E-01	7.41E-01	7.40E-01	7.39E-01	7.38E-01	7.45E-01	7.49E-01	7.52E-01	7.56E-01	7.61E-01	7.36E-01
CDp1	1.89E-02	1.71E-02	1.55E-02	1.47E-02	1.51E-02	1.64E-02	1.76E-02	1.86E-02	1.95E-02	2.00E-02	2.15E-02	2.25E-02
CDp2	-8.74E-05	-7.73E-05	-5.04E-05	-3.75E-05	-2.90E-05	-1.92E-05	-1.43E-05	-1.12E-05	-9.62E-06	-8.27E-06	-7.39E-06	-6.86E-06
CDp	1.88E-02	1.71E-02	1.55E-02	1.46E-02	1.50E-02	1.64E-02	1.76E-02	1.86E-02	1.95E-02	2.00E-02	2.15E-02	2.25E-02
CDi	3.40E-02	3.40E-02	3.40E-02	3.36E-02	3.26E-02	3.09E-02	2.98E-02	2.88E-02	2.79E-02	2.71E-02	2.59E-02	2.39E-02
CD	5.27E-02	5.10E-02	4.95E-02	4.83E-02	4.76E-02	4.73E-02	4.74E-02	4.74E-02	4.74E-02	4.71E-02	4.74E-02	4.64E-02
CL(near-field)	7.46E-01	7.46E-01	7.46E-01	7.46E-01	7.46E-01	7.46E-01	7.46E-01	7.46E-01	7.46E-01	7.46E-01	7.46E-01	7.46E-01
CD(near-field)	4.57E-02	4.57E-02	4.57E-02	4.57E-02	4.57E-02	4.57E-02	4.57E-02	4.57E-02	4.57E-02	4.57E-02	4.57E-02	4.57E-02
CL(%)	99.56	99.25	99.22	99.12	98.99	98.90	99.83	100.34	100.78	101.24	101.90	98.60
CDp(%)	41.11	37.35	33.89	32.07	32.89	35.84	38.57	40.77	42.74	43.72	47.04	49.29
CDi(%)	74.34	74.40	74.39	73.62	71.41	67.71	65.20	63.07	61.12	59.43	56.63	52.40
CD(%)	115.45	111.75	108.29	105.69	104.30	103.55	103.76	103.84	103.87	103.15	103.67	101.70

Table 3 Variations of drag and lift coefficients of a NACA0012 wing model due to the wake integral stations.

AoA = 12 deg	Wake Integral Station (*x* chords departed from the end of the wing section)											
	0	0.1	0.2	0.5	1	2	3	4	5	6	8	10
CL	8.90E-01	8.89E-01	8.88E-01	8.87E-01	8.87E-01	8.85E-01	8.94E-01	9.00E-01	9.03E-01	9.06E-01	8.93E-01	8.71E-01
CDp1	2.22E-02	1.94E-02	1.86E-02	1.76E-02	1.76E-02	2.12E-02	2.31E-02	2.49E-02	2.59E-02	2.71E-02	2.94E-02	3.06E-02
CDp2	-1.16E-04	-9.26E-05	-6.99E-05	-5.12E-05	-5.12E-05	-2.89E-05	-2.20E-05	-1.84E-05	-1.54E-05	-1.38E-05	-1.23E-05	-1.12E-05
CDp	2.21E-02	1.93E-02	1.86E-02	1.75E-02	1.75E-02	2.12E-02	2.30E-02	2.48E-02	2.59E-02	2.70E-02	2.94E-02	3.06E-02
CDi	4.89E-02	4.89E-02	4.88E-02	4.81E-02	4.81E-02	4.36E-02	4.18E-02	4.03E-02	3.90E-02	3.80E-02	3.52E-02	3.26E-02
CD	7.10E-02	6.82E-02	6.74E-02	6.56E-02	6.56E-02	6.48E-02	6.49E-02	6.52E-02	6.49E-02	6.50E-02	6.46E-02	6.32E-02
CL(near-field)	8.94E-01	8.94E-01	8.94E-01	8.94E-01	8.94E-01	8.94E-01	8.94E-01	8.94E-01	8.94E-01	8.94E-01	8.94E-01	8.94E-01
CD(near-field)	6.13E-02	6.13E-02	6.13E-02	6.13E-02	6.13E-02	6.13E-02	6.13E-02	6.13E-02	6.13E-02	6.13E-02	6.13E-02	6.13E-02
CL(%)	99.57	99.44	99.32	99.24	99.24	99.00	99.98	100.65	101.00	101.29	99.89	97.48
CDp(%)	36.00	31.43	30.26	28.61	28.61	34.55	37.57	40.52	42.25	44.11	47.95	49.96
CDi(%)	79.81	79.79	79.58	78.41	78.41	71.18	68.22	65.75	63.54	61.92	57.46	53.17
CD(%)	115.82	111.22	109.84	107.02	107.02	105.72	105.79	106.26	105.80	106.02	105.41	103.13

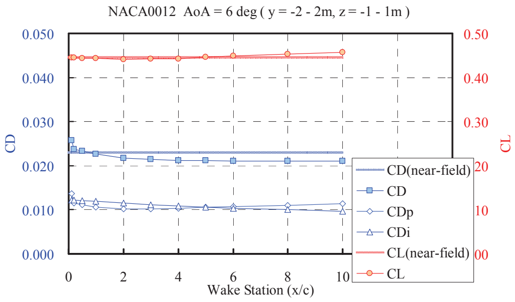

Fig. 7 Variations of drag and lift coefficients of a NACA0012 wing model due to the wake integral stations (AoA = 6deg).

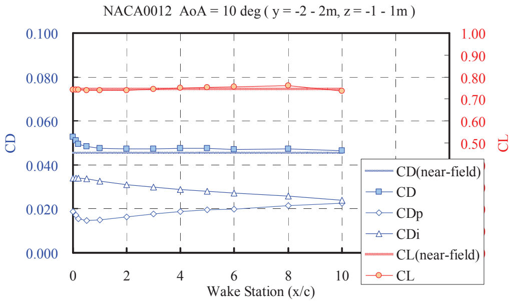

Fig. 8 Variations of drag and lift coefficients of a NACA0012 wing model due to the wake integral stations (AoA = 10deg).

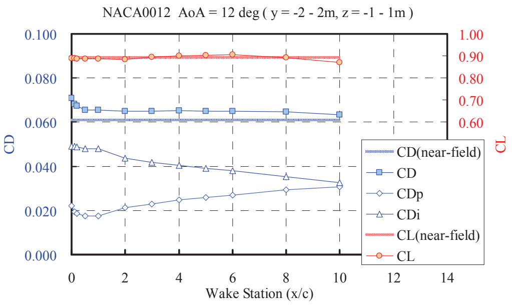

Fig. 9 Variations of drag and lift coefficients of a NACA0012 wing model due to the wake integral stations (AoA = 12deg).

3.4.2 Drag Component Distribution

Examples of the distribution of aerodynamic force component “fragments” and their spanwise distributions are shown in Fig. 10 to Fig. 13. These are the results at an angle of attack of 6 deg and the wake integral stations are at 1 and 10 chord lengths downstream from the trailing edge. The integrated aerodynamic forces are the integral of the fragments. Thus, the spanwise distributions are the normal-directional integrals of the fragments and the total forces are the integrals of the spanwise distributions. The rectangular shadow extending from the center of the left edge of the contour plot is the wing model, which is seen transparently through the contour plot from downstream.

The aerodynamic drags are chiefly observed inside the trailing vortex. Downstream of the wing’s trailing edge, the kinetic energy of the vortex decays by shearing in the vortex core. The lift force is computed as the cumulative sum of vorticity and the spanwise distribution stands up at the trailing vortex. It is seen that the vortex lines are connected through the wing span. As the wake integral station moves downstream, the trailing edge vortex core becomes larger and the increase of aerodynamic lift around the vortex spreads.

These observed aerodynamic force distribution characteristics conform to our physical intuition about the flow around a simple rectangular wing at low-speed. Thus, our wake integral software is considered to be validated for low speeds.

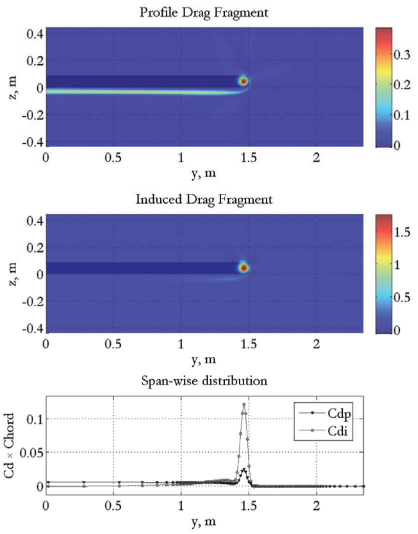

Fig. 10 Profile and induced drag distribution at 1 chord downstream from the trailing edge with the angle of attack of 6 deg.

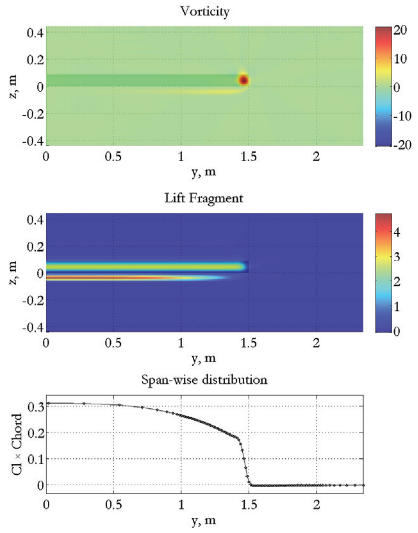

Fig. 11 Vorticity and lift distribution at 1 chord downstream from the trailing edge with the angle of attack of 6 deg.

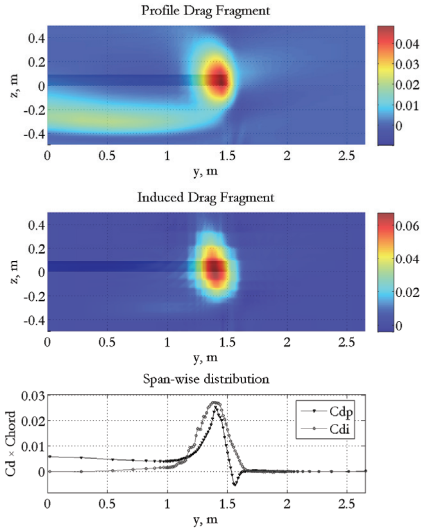

Fig. 12 Profile and induced drag distribution at 10 chord downstream from the trailing edge with the angle of attack of 6 deg.

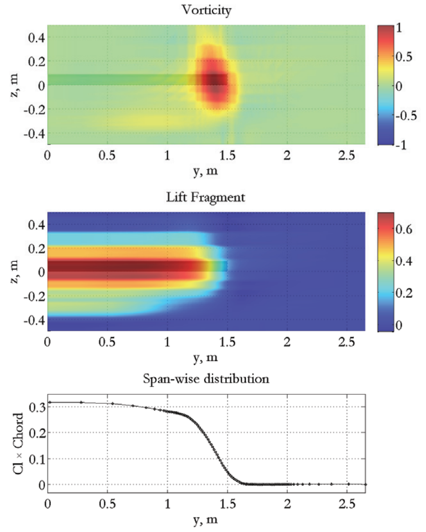

Fig. 13 Vorticity and lift distribution at 10 chord downstream from the trailing edge with the angle of attack of 6 deg.

3.5 Grid Dependency

As seen in the aerodynamic force distributions, the profile and induced drag originate in the vortical region of the wake. The lift is also strongly dependent on the vortices. On the other hand, regions without vortices have less influence on aerodynamic force production. To reduce computation cost while maintaining accuracy, an inhomogeneous grid was investigated.

In the present analysis, the WIM computation was performed using data mapped on rectangular mesh nodes from a wake survey plane which was cut from the three-dimensional CFD spatial data. Because a Poisson equation on vorticity has to be solved, a finer computational mesh is required to improve the precision of the induced drag computation. The dependency of the output on the number of mesh points is shown in Fig. 14. Four levels of mesh refinement (Coarse, Medium, Fine, and Minute) were used as shown in Fig. 15. From Fig. 14, we can see that lift coefficient is little affected by the number of mesh points while drag coefficient is highly dependent on it. It should be noted that a finer mesh makes the induced drag larger because it can capture small vortices (Fig. 16). On the other hand, a larger mesh overestimates profile drag because local total pressure losses are spread over a large mesh area.

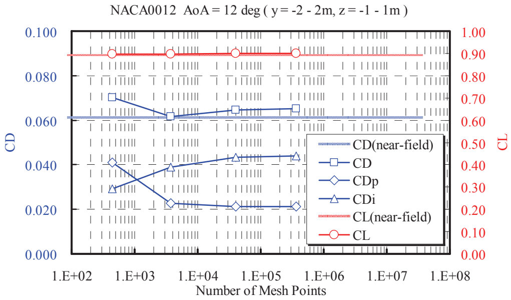

Fig. 14 Aerodynamic force dependency to number of mesh points.

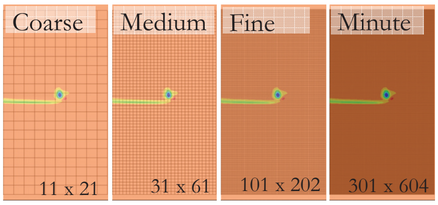

Fig. 15 Images of meshes put over total pressure loss contours

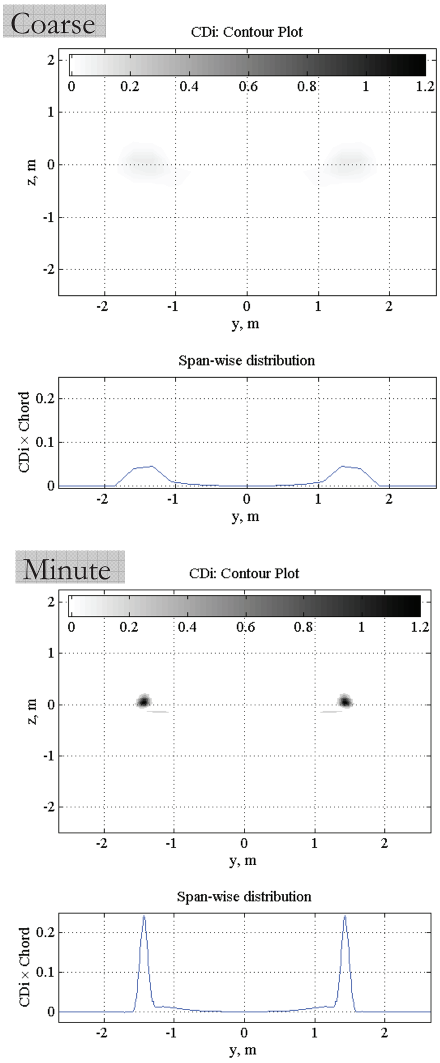

Fig. 16 Induced drag variation due to mesh refinement (square mesh).

While finer meshes certainly improve the precision of aerodynamic force computation, increasing fineness leads to an exponentially increasing computational cost (Fig. 17). Therefore, the internal logic of the program was changed to support an oblong mesh to suppress computational cost (Fig. 18). Thus, precise computation of drag was realized with a lower dependency on the mesh fineness (Fig. 19) because of local mesh refinement around drag-producing factors such as vortices (Fig. 20). All the analyses in this report were performed using oblong meshes.

When an ordered WIM mesh is used, in general the CFD grid points will not coincide with the mesh nodes, requiring interpolation when mapping the CFD data onto the mesh with a resulting loss of precision. To further improve precision, an unordered mesh should be used.

However, the software version used in this study assumes a structured mesh system and will have to be rewritten to support unordered meshes. This may be a task for later development.

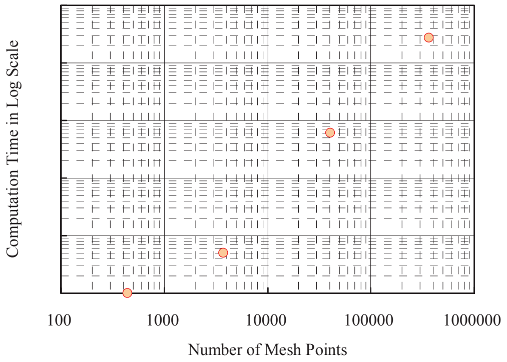

Fig. 17 Computation time depend on number of mesh points.

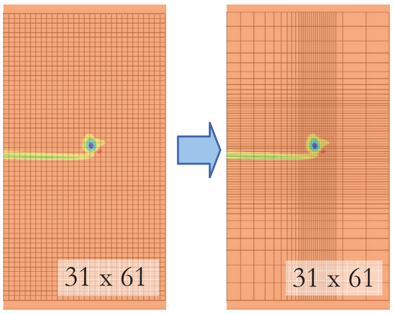

Fig. 18 Introduction of oblong mesh.

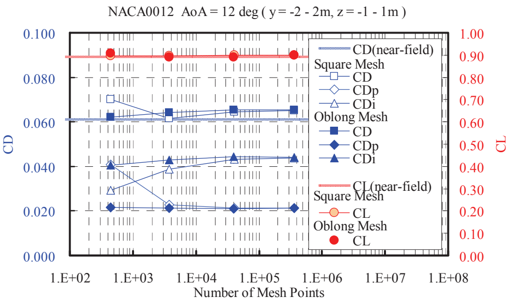

Fig. 19 Comparison between square mesh and oblong mesh.

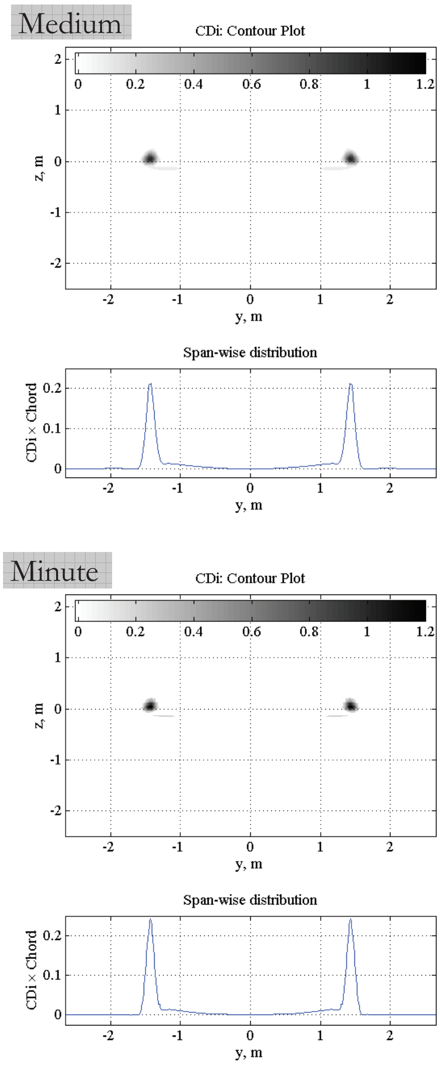

Fig. 20 Induced drag variation due to mesh refinement using oblong mesh.

4 DLR F6 at Transonic Speed

4.1 Model Description

The DLR F6 model was next used to validate the software at transonic speed. The DLR F6 is a target model used in the 3rd AIAA drag prediction workshop[13] (AIAA-DPW), and is a wing-body model with a mean aerodynamic chord (MAC) and projected half span of 141.2mm and 585.647 mm, respectively, and a reference area of 72700 mm^2. Details of the geometry are described on the drag prediction workshop website[14].

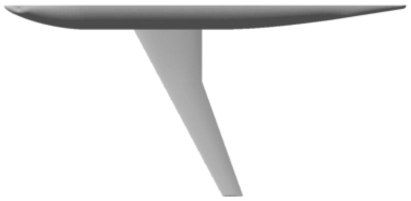

Fig. 21 Planform image of DLR F6 model.

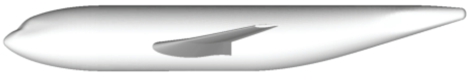

Fig. 22 Sideview image of DLR F6 model.

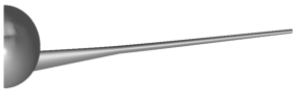

Fig. 23 Frontview image of DLR F6 model.

4.2 CFD Conditions

The computation was performed when JAXA attended the 3rd AIAA DPW15). The Mach number, static temperature, and Reynolds number of the computations were 0.75, 322.22 K, and 5.0 × 10^6, respectively. The computational mesh was a structured mesh and the UPACS solver was used. The angles of attack were -3.0, -2.0, -1.0, -0.5, 0.0, 0.5, 1.0, and 1.5.

4.3 Wake Integral Conditions

WIM analysis planes were chosen perpendicular to the free-stream direction and set at 3, 5, 7, and 9 times the MAC downstream from the model center, which is located at 2.46 MAC downstream from the nose of the body. The entropy increment contour image at each plane is illustrated in Fig. 24. The two planes furthest upstream intersect the body of the model.

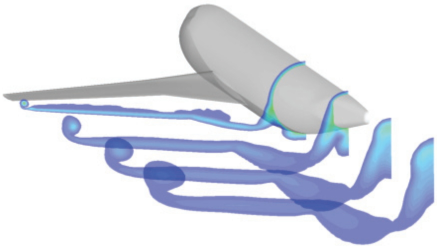

Fig. 24 Image of entropy increment contour at each WIM analysis plane.

As with the low-speed rectangular wing above, the total pressure upstream of the DLR F6 model is not uniform. However, the subtraction of upstream flow properties used in the simple rectangular wing case cannot be applied to this case because this model has a complex configuration and the flow around the model is complicated. Thus, the eddy viscosity was used to determine the wake area and $(\mu_l + \mu_t)/\mu_l$ was used as a threshold value, where μ_l and μ_t are the dynamic and eddy viscosities, respectively16). A threshold value of 11 was used because the total aerodynamic force was closest to the near-field result with that value. The threshold value determination problem will be discussed in Section 4.5 below. Because the flow in this case is transonic, eddy viscosity alone is insufficient to determine the wake area due to the shock wave. To capture the flow behind the shock wave, the entropy increment value at the edge of the shock determined by the "shock function" $(U \cdot \nabla p)/(a\|\nabla p\|)$ was used. The threshold value of it was determined to be 0.004.

4.4 Analysis Results

4.4.1 Total Value

An example of streamwise variation of the WIM analysis is tabulated in Table 4 and plotted in Fig. 25. When the WIM plane intersects the model body, the plane cannot capture the separation of flow from the body and the WIM profile drag seems not to account for all of the profile drag component. In transonic flow, replacement of induced drag with profile drag is relatively small and is not noticeable.

The lift and the drag computed at the plane 7 MAC downstream from the model center are plotted against angle of attack in Fig. 26. While lift and total drag agree very well with the surface integral values, the drag value and its slope are somewhat less.

Table 4 WIM analysis results of DLR F6 at the AoA of 1.0 deg.

	xMAC downstream			
	3	5	7	9
CL	5.55E-01	5.88E-01	5.96E-01	5.97E-01
CDp1	1.81E-02	2.13E-02	2.11E-02	2.10E-02
CDp2	-9.19E-04	-7.87E-04	-4.93E-04	-3.80E-04
CDp	1.72E-02	2.05E-02	2.07E-02	2.06E-02
CDi	1.23E-02	1.21E-02	1.18E-02	1.14E-02
CD	2.95E-02	3.26E-02	3.25E-02	3.19E-02
CL(near-field)	5.97E-01	5.97E-01	5.97E-01	5.97E-01
CD(near-field)	3.30E-02	3.30E-02	3.30E-02	3.30E-02
CL(%)	92.90	98.58	99.88	99.94
CDp(%)	51.99	62.14	62.55	62.33
CDi(%)	37.21	36.70	35.76	34.38
CD(%)	89.20	98.84	98.31	96.71

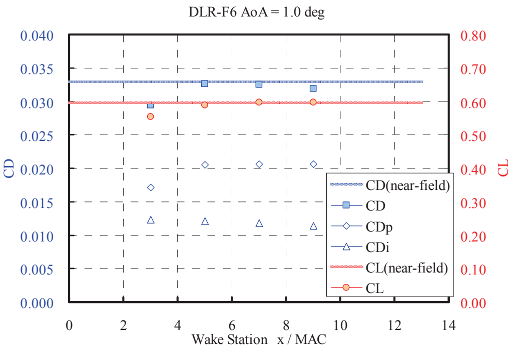

Fig. 25 WIM analysis results of DLR F6 at the AoA of 1.0 deg.

AoA	-3	-2	-1	-0.5	0	0.5	1	1.5
CL(near-field)	1.32E-01	2.49E-01	3.64E-01	4.22E-01	4.80E-01	5.38E-01	5.97E-01	6.55E-01
CL(wake)	1.22E-01	2.48E-01	3.60E-01	4.20E-01	4.79E-01	5.37E-01	5.96E-01	6.55E-01
CD(near-field)	1.90E-02	2.06E-02	2.33E-02	2.51E-02	2.72E-02	2.98E-02	3.30E-02	3.74E-02
CD(wake)	1.91E-02	2.07E-02	2.33E-02	2.50E-02	2.70E-02	2.95E-02	3.25E-02	3.61E-02
CDp	1.78E-02	1.80E-02	1.84E-02	1.87E-02	1.91E-02	1.98E-02	2.07E-02	2.21E-02
CDi	1.29E-03	2.68E-03	4.85E-03	6.28E-03	7.91E-03	9.74E-03	1.18E-02	1.40E-02

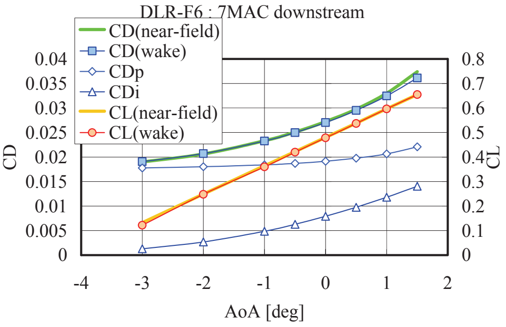

Fig. 26 Lift and drag at 7MAC downstream plane plotted against angle of attack.

4.4.2 Aerodynamic Force Distribution

Here, we discuss aerodynamic force distributions over the DLR F6 model as well as for the NACA0012 rectangular wing. As an example, data at an angle of attack of 1 deg are shown. The profile and the induced drag distribution at 3 MAC downstream from the model center are shown in Fig. 27, and the vorticity and the lift distribution are shown in Fig. 28. Although the precise profile drag exerted on the body could not be computed at the analysis planes that intersected the model's body, the obtained aerodynamic force distribution is still informative.

At the plane close to the main wing, the induced drag component is strongly shed from the wing tip. On the other hand, profile drag is produced around the joint between the body and the main wing. Interference drag seems to make up a large part of profile drag and is as large as the induced drag produced by the trailing vortex. This shows that a device that reduces interference drag can give a reduction on the total airplane drag similarly to the effect on a winglet on induced drag. Although a shock wave exists upon the main wing and should be captured in the profile drag, it cannot be seen in the contour plot.

Lift force is large over the inner wing with longer chord length. The body is an obstacle to the vortices connected from one side to the other side of the main wing and lift is relatively lower at the body (Fig. 28).

When the analysis plane reaches 7 MAC downstream from the model center, the radius of the trailing vortex is larger and the drag resolution is degraded, although the trend of the aerodynamic force distribution remains (Fig. 29). As in the low-speed rectangular wing case, moving downstream the vortex spreads and steepness of the drag and lift distributions at the wing tip also spread. The interference drag component of the profile drag was merged with the drag due to separation at the tail of the body.

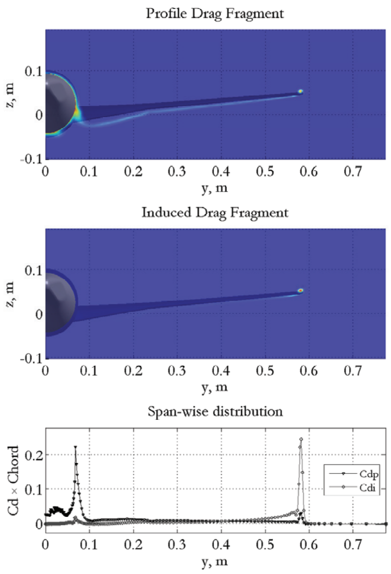

Fig. 27 Profile and induced drag distribution at 3 MAC downstream from the model center with the angle of attack of 1 deg.

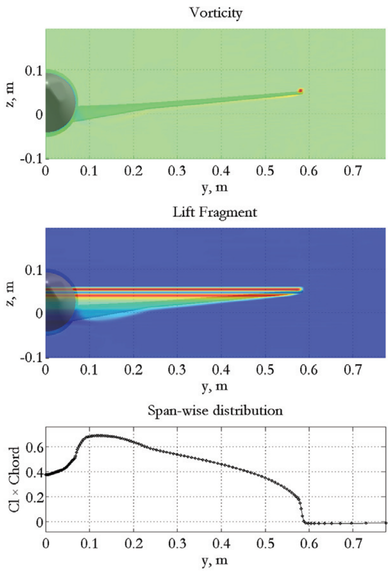

Fig. 28 Vorticity and lift distribution at 3 MAC downstream from the model center with the angle of attack of 1 deg.

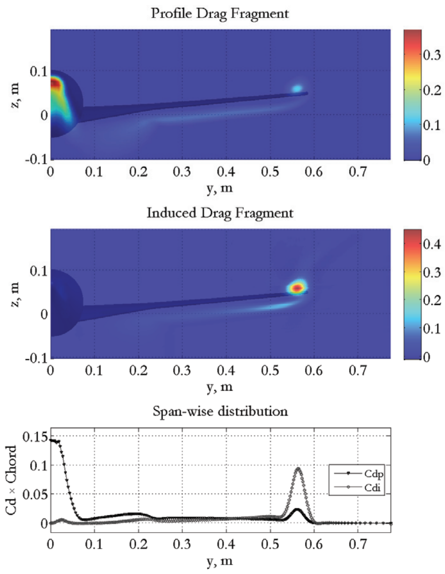

Fig. 29 Profile and induced drag distribution at 7 MAC downstream from the model center with the angle of attack of 1 deg.

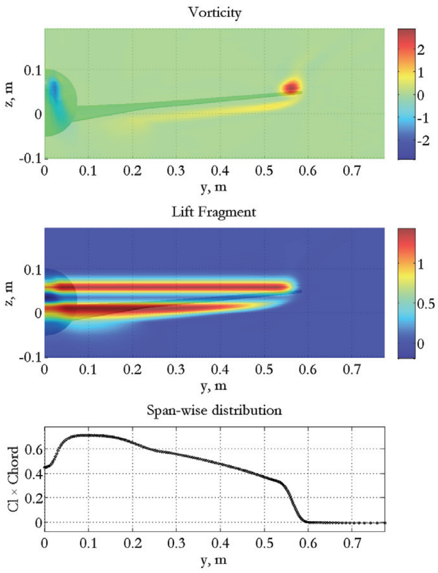

Fig. 30 Vorticity and lift distribution at 7 MAC downstream from the model center with the angle of attack of 1 deg.

4.5 Wake Area Determination

Determining the area occupied by the wake is a large problem when acquiring precise aerodynamic force by the WIM, especially when using CFD data because CFD spatial data are intrinsically contaminated by a numerical error known as spurious drag[12)16)]. Examples of wake area variation according to eddy viscosity threshold values are shown in Fig. 31, and the variations in drag resulting from the changing threshold values are shown in Fig. 32. The same data are plotted against the eddy viscosity in Fig. 33 and the best threshold value was determined as the value at which the computed drag value is the closest to the near-field value.

The arbitrariness of the threshold value to determine the wake behind the shock is a problem. As stated in the Section 4.3, the threshold value was determined by the entropy increment at the edge of the shock. However, the entropy increment should be originally zero at the outside of the shock. This means that this threshold determination depends on the spurious entropy increment. An improved method to determine the wake area considering the shock is required.

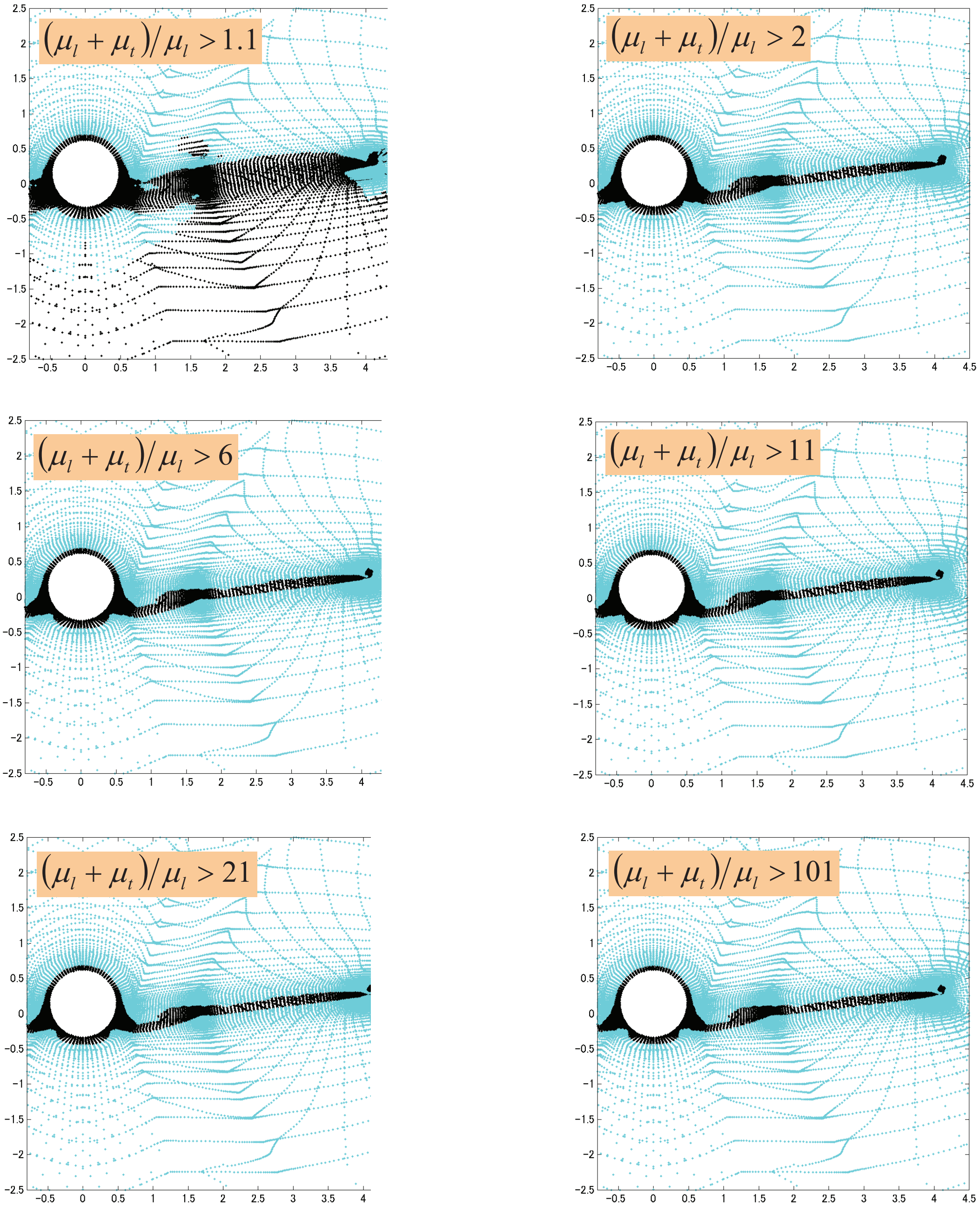

Fig. 31 Example of wake area (AoA = 1.5 deg, 3MAC downstream; blue area is the wake area).

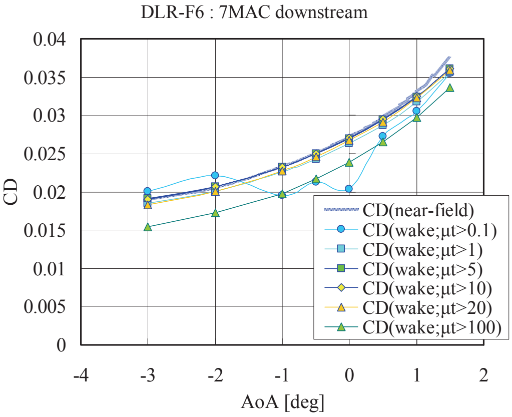

Fig. 32 Drag coefficient variation due to eddy viscosity threshold change

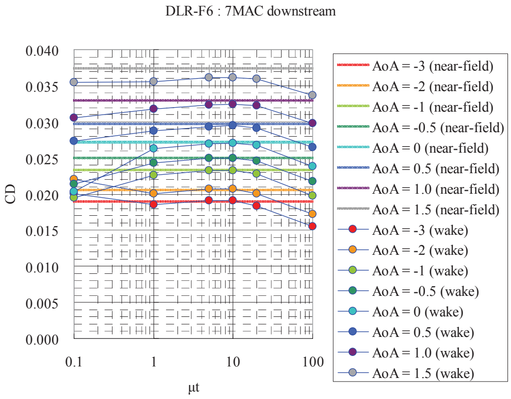

Fig. 33 Drag coefficient dependency on eddy viscosity threshold value.

5 Conclusions

Wake integral method (WIM) analysis was performed on the CFD flow data around a low-speed rectangular wing and a transonic DLR F6 model. The software developed for the WIM analysis succeeded in extracting the total and distributed drag and lift, and in drag decomposition. The lift force fragment representation which is easy to be integrated was evolved and taken into the software. Aerodynamic force distribution and drag component decomposition can provide insights into aerodynamic force production.

The WIM can be applied to both CFD and wind tunnel data. Therefore, further studies employing experimental data and comparison with computational data are planned to improve experimental and numerical drag analysis and to accelerate the airplane design process.

Acknowledgments

The authors would like to thank Dr. Mitsuhiro Murayama and Taro Imamura for their kindness in providing the CFD data used in this research.

Bibliography

1) Chapman, D.R., Mark, H., and Pirtle, M.W., “Computers vs. Wind Tunnels for Aerodynamic Flow Simulations,” Astronautics & Aeronautics, pp. 22-35, Apr, 1975.

2) Betz, A., “A Method for the Direct Determination of Profile Drag,” Zeitschrift für Flugtechnik und Motorluftschiffahrt, Vol. 16, 1925, pp.42-44. (In German.)

3) Maskell, E.C., “Progress Towards a Method for the Measurement of the Components of the Drag of a Wing of Finite Span,” RAE Technical Report 72232, 1972.

4) Cummings, R.M., Giles, M.B., and Shrinivas, G.N., “Analysis of the Elements of Drag in Three-Dimensional Viscous and Inviscid Flows,” AIAA 96-2482-CP, 1996.

5) Nikfetrat, K., van Dam, C.P., Vijgen, P.M.H.W., and Chang, I.C., “Prediction of Drag at Subsonic and Transonic Speeds Using Euler Methods,” AIAA 92-0169, Jan. 1992.

6) Kusunose, K, “A Wake Integration Method for Airplane Drag Prediction,” The 21st Century COE Program International COE of Flow Dynamics Lecture Series Volume 3, Tohoku University Press, 2005.

7) Méheut, M. and Bailly, D., “Profile Drag Formulations and Drag Breakdown from Wake Measurements,” AIAA 2006-3166, 2006.

8) Ueno, M., Fujieda, H., Iwasaki, A., and Fujita, T., “Aerodynamic Characteristics Prediction from Wake Survey Data Using Five-Hole Pressure Probes,” Proceedings of 30th annual meeting of Japan Society for Aeronautical and Space Sciences, 1999. (In Japanese.)

9) Ueno, M., Fujita, T, and Iwasaki, A, “Estimation of Aerodynamic Characteristics Using Wake Integral Method at the NAL 2m × 2m Gust Wind Tunnel,” Proceedings of 31st annual meeting of Japan Society for Aeronautical and Space Sciences, 2000. (In Japanese.)

10) Imamura, T., Enomoto, S., and Yamamoto, K., “Noise Generation around NACA0012 Wingtip using Large-Eddy-Simulation,” 25th Congress of the International Council of the Aeronautical Sciences (ICAS), Hamburg, Germany, 3 Sep. 2006.

11) Yates, J.E. and Donaldson, C.duP., “A Fundamental Study of Drag and an Assessment of Conventional Drag-Due-to-Lift Reduction Devices,” NASA CR-4004, Sep. 1986.

12) Destarac, “Far-Field / Near-Field Drag Balance and Application of Drag Extracion in CFD,” von Karman Institute for Fluid Dynamics Lecture Series 2003-02, CFD-BASED AIRCRAFT DRAG PREDICTION AND REDUCTION, Brussels, Belgium, Feb. 2003.

13) Vassbert, J.C., Tinoco., E.N., Mani, M., Brodersen, O.P., Eisfeld, B., Wahls, R.A., Morrison, J.H., Zickuhr, T., Laflin, K.R., Mavriplis, D.J., “Summary of the Third AIAA CFD Drag Prediction Workshop,” AIAA 2007-260, Jan. 2007.

14) Geometries page of 3rd AIAA Drag Prediction Workshop, http://aaac.larc.nasa.gov/tsab/cfdlarc/aiaa-dpw/Workshop3/DPW3-geom.html, web site.

15) Murayama, M. and Yamamoto, K., “Comparison Study of Drag Prediction for the 3rd CFD Drag Prediction Workshop by Structured and Unstructured Mesh Method,” AIAA Paper 2007-0258, Jan. 2007.

16) Paparone, L., and Tognaccini, R., "Computational Fluid Dynamics-Based Drag Prediction and Decomposition, AIAA Journal, Vol.41, No.9, Sep, 2003.

JAXA Research and Development Report JAXA-RR-07-030E

Date of Issue : February 29, 2008
Edited and Published by : Japan Aerospace Exploration Agency
7-44-1 Jindaiji-higashimach, Chofu-shi,Tokyo 182-8522,Japan
URL : http://www.jaxa.jp/
Printed by : NORTH ISLAND Co.,Ltd

Inquires about copyright and reproduction should be addressed to the Aerospace Information Archive Center, Information Systems Department, JAXA.
2-1-1 Sengen, Tsukuba-shi, Ibaraki 305-8505, Japan
Phone : +81-29-868-5000 Fax : +81-29-868-2956

Copyright © 2008 by JAXA.

All rights reserved. No part of this publication may be reproduced, stored in retrieval system or transmitted, in any form or by any means, electoronic, mechanical, photocopying, recording, or otherwise, without permission in writing form the publisher.

Japan Aerospace
Exploration Agency

Printed on Recycled Paper